

PlenOctrees for Real-time Rendering of Neural Radiance Fields

Alex Yu¹
Hao Li^{1,3}

Ruilong Li^{1,2}
Ren Ng¹

Matthew Tancik¹
Angjoo Kanazawa¹

¹UC Berkeley

²USC Institute for Creative Technologies

³Pinscreen

Abstract

We introduce a method to render Neural Radiance Fields (NeRFs) in real time using PlenOctrees, an octree-based 3D representation which supports view-dependent effects. Our method can render 800×800 images at more than 150 FPS, which is over 3000 times faster than conventional NeRFs. We do so without sacrificing quality while preserving the ability of NeRFs to perform free-viewpoint rendering of scenes with arbitrary geometry and view-dependent effects. Real-time performance is achieved by pre-tabulating the NeRF into a PlenOctree. In order to preserve view-dependent effects such as specularities, we factorize the appearance via closed-form spherical basis functions. Specifically, we show that it is possible to train NeRFs to predict a spherical harmonic representation of radiance, removing the viewing direction as an input to the neural network. Furthermore, we show that PlenOctrees can be directly optimized to further minimize the reconstruction loss, which leads to equal or better quality compared to competing methods. Moreover, this octree optimization step can be used to reduce the training time, as we no longer need to wait for the NeRF training to converge fully. Our real-time neural rendering approach may potentially enable new applications such as 6-DOF industrial and product visualizations, as well as next generation AR/VR systems. PlenOctrees are amenable to in-browser rendering as well; please visit the project page for the interactive online demo, as well as video and code: <https://alexyu.net/plenoctrees>.

1. Introduction

Despite the progress of real-time graphics, interactive 3D content with truly photorealistic scenes and objects are still time consuming and costly to produce due to the necessity of optimized 3D assets and dedicated shaders. Instead, many graphics applications opt for image-based solutions. E-commerce websites often use a fixed set of views to showcase their products; VR experiences often rely on 360

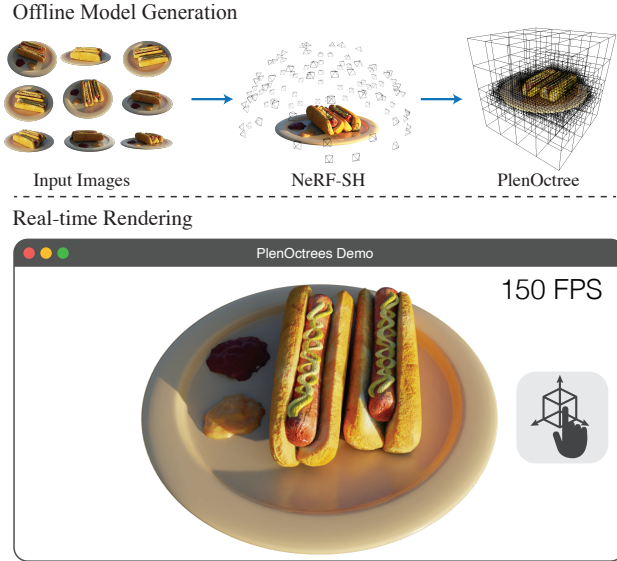


Figure 1: **Real-time NeRF with PlenOctrees.** Given a set of posed images of a scene, our method creates a 3D volumetric model that can be rendered in real-time. We propose PlenOctrees, which are octrees that can capture view-dependent effects such as specularities. Rendering using our approach is orders of magnitude faster than NeRF.

video recordings to avoid the costly production of real 3D scenes, and mapping services such as Google Street View stitch images into panoramic views limited to 3-DOF.

Recent advances in neural rendering, such as neural volumes [22] and neural radiance fields (NeRFs) [28], open a promising new avenue to model arbitrary objects and scenes in 3D from a set of calibrated images. NeRFs in particular can faithfully render detailed scenes and appearances with non-Lambertian effects from any view, while simultaneously offering a high degree of compression in terms of storage. Partly due to these exciting properties, of late, there has been an explosion of research based on NeRF.

Nevertheless, for practical applications, runtime performance remains a critical limitation of NeRFs: due to the extreme sampling requirements and costly neural network queries, rendering a NeRF is agonizingly slow. For illustration, it takes roughly 30 seconds to render an 800×800

image from a NeRF using a high performance GPU, making it impractical for real-time interactive applications.

In this work, we propose a method for rendering a NeRF in real time, achieved by distilling the NeRF into a hierarchical 3D volumetric representation. Our approach preserves NeRF’s ability to synthesize arbitrarily complex geometry and view-dependent effects from any viewpoint and requires no additional supervision. In fact, our method achieves and in many cases surpasses the quality of the original NeRF formulation, while providing significant acceleration. Our model allows us to render an 800x800 image at 167.68 FPS on a NVIDIA V100 GPU and does not rely on a deep neural network during test time. Moreover, our representation is amenable to modern web technologies, allowing interactive rendering in a browser on consumer laptops.

Naive NeRF rendering is slow because it requires dense sampling of the scene, where every sample requires inference through a deep MLP. Because these queries depend on the viewing direction as well as the spatial position, one cannot naively cache these color values for all viewing directions.

We overcome these challenges and enable real-time rendering by pre-sampling the NeRF into a tabulated view-dependent volume which we refer to as a PlenOctree, named after the plenoptic functions of Adelsen and Bergen [1]. Specifically, we use a sparse voxel-based octree where every leaf of the tree stores the appearance and density values required to model the radiance at a point in the volume. In order to account for non-Lambertian materials that exhibit view-dependent effects, we propose to represent the RGB values at a location with spherical harmonics (SH), a standard basis for functions defined on the surface of the sphere. The spherical harmonics can be evaluated at arbitrary query viewing directions to recover the view dependent color.

Although one could convert an existing NeRF into such a representations via projection onto the SH basis functions, we show that we can in fact modify a NeRF network to predict appearances explicitly in terms of spherical harmonics. Specifically, we train a network that produces coefficients for the SH functions instead of raw RGB values, so that the predicted values can later be directly stored within the leaves of the PlenOctree. We also introduce a sparsity prior during NeRF training to improve the memory efficiency of our octrees, consequently allowing us to render higher quality images. Furthermore, once the structure is created, the values stored in PlenOctree can be optimized because the rendering procedure remains differentiable. This enables the PlenOctree to obtain similar or better image quality compared to NeRF. Our pipeline is illustrated in Fig. 2.

Additionally, we demonstrate how our proposed pipeline can be used to accelerate NeRF model training, making our solution more practical to train than the original NeRF ap-

proach. Specifically, we can stop training the NeRF model early to convert it into a PlenOctree, which can then be trained significantly faster as it no longer involves any neural networks.

Our experiments demonstrate that our approach can accelerate NeRF-based rendering by 5 orders of magnitude without loss in image quality. We compare our approach on standard benchmarks with scenes and objects captured from 360° views, and demonstrate state-of-the-art level performance for image quality and rendering speed.

Our interactive viewer can enable operations such as object insertion, visualizing radiance distributions, decomposing the SH components, and slicing the scene. We hope that these real-time operations can be useful to the community for visualizing and debugging NeRF-based representations.

To summarize, we make the following contributions:

- The first method that achieves real-time rendering of NeRFs with similar or improved quality.
- NeRF-SH: a modified NeRF that is trained to output appearance in terms of spherical basis functions.
- PlenOctree, a data structure derived from NeRFs which enables highly efficient view-dependent rendering of complex scenes.
- Accelerated NeRF training method using an early training termination, followed by a direct fine-tuning process on PlenOctree values.

2. Related Work

Novel View Synthesis. The task of synthesizing novel views of a scene given a set of photographs is a well-studied problem with various approaches. All methods predict an underlying geometric or image-based 3D representation that allows rendering from novel viewpoints. Mesh based methods represent the scene with surfaces, and have been used to model Lambertian (diffuse) [53] and non-Lambertian scenes [57, 5, 3].

Mesh based representations are compact and easy to render; however, optimizing a mesh to fit a complex scene of arbitrary topology is challenging. Image-based rendering methods [17, 40, 57], on the other hand, enable easy capture as well as photo-realistic and fast rendering, however are often bounded in the viewing angle and do not allow easy editing of the underlying scene.

Volume rendering is a classical technique with a long history of research in the graphics community [7]. Volume-based representations such as voxel grids [39, 16, 22, 12, 52, 41] and multi-plane images (MPIs) [46, 33, 61, 45, 27] are a popular alternative to mesh representations due to their topology-free nature: gradient-based optimization is therefore straightforward, while rendering can still be real-time.

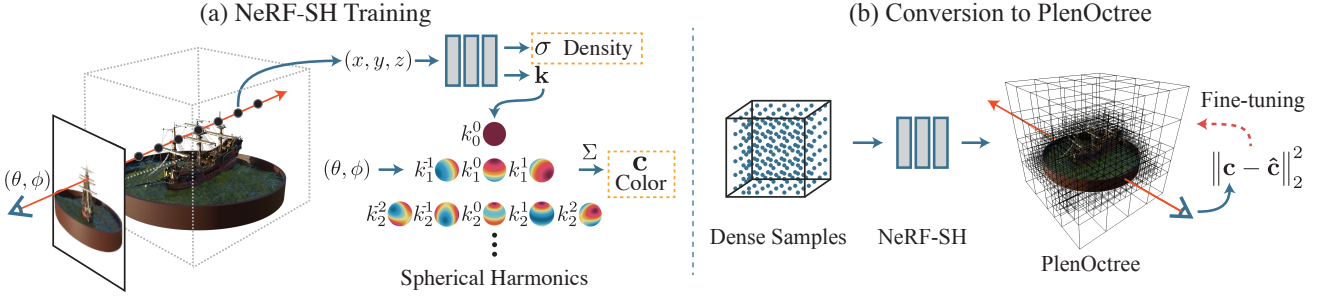


Figure 2: Method Overview. We propose a method to quickly render NeRFs by training a modified NeRF model (NeRF-SH) and converting it into a PlenOctree, an octree that captures view-dependent effects. a) The NeRF-SH model uses the same optimization procedure and volume rendering method presented in NeRF [28]. However, instead of predicting the RGB color c directly, the network predicts spherical harmonic coefficients k . The color c is calculated by summing the weighted spherical harmonic bases evaluated at the corresponding ray direction (θ, ϕ) . The spherical harmonics enable the representation to model view-dependent appearance. The values in the orange boxes are used for volume rendering. b) To build a PlenOctree, we densely sample the NeRF-SH model in the volume around the target object and tabulate the density and SH coefficients. We can further optimize the PlenOctree directly with the training images to improve its quality.

However, such naive volumetric representations are often memory bound, limiting the maximum resolution that can be captured. Volumetric octrees are a popular approach for reducing memory and compute in such cases. We refer the reader to this survey [15] for a historical perspective on octree volume rendering. Octrees have been used in recent work to decrease the memory requirements during training for other 3D tasks [36, 10, 49, 54]. Concurrent with this work, Nex [56] extends MPIS to encode spherical basis functions that enable view-dependent rendering effects in real-time. However, unlike our representation, their approach is limited in the viewing direction due to their use of MPIS. Also concurrently, Lombardi et al. [23] propose to model data using geometric primitives, which allows for fast rendering while conserving space; however, they require a coarse mesh to initialize the primitives.

Coordinate-Based Neural Networks. Recently, coordinate-based neural networks have emerged as a popular alternative to explicit volumetric representations, as they are not limited to a fixed voxel representation. These methods train a multilayer perceptron (MLP) whose input is a coordinate and output is some property of space corresponding to that location. These networks have been used to predict occupancy [26, 4, 32, 37, 29, 18], signed distance fields [30, 9, 58, 59], and radiance [28]. Coordinate-based neural networks have been used for view synthesis in Scene Representation Networks [42], NeRFs [28], and many NeRF extensions [25, 31, 38, 44]. These networks represent a continuous function that can be sampled at arbitrarily fine resolutions without increasing the memory footprint. Unfortunately, this compactness is achieved at the expense of computational efficiency as each sample must be processed by a neural network. As a result, these representations are often slow and impractical for

real-time rendering.

NeRF Accelerations. While NeRFs are able to produce high quality results, their computationally expensive rendering leads to slow training and inference. One way to speed up the process of fitting a NeRF to a new scene is to incorporate priors learned from a dataset of similar scenes. This can be accomplished by conditioning on predicted image features [50, 60, 55] or meta-learning [48]. To improve inference speed, Neural Sparse Voxel Fields (NSVF) [21] learns a sparse voxel grid of features that are input into a NeRF like model. The sparse voxel grid allows the renderer to skip over empty regions when tracing a ray which improves the render time $\sim 10x$. Decomposed Radiance Fields [35] spatially decomposes a scene into multiple smaller networks. This method focuses on forward facing scenes. AutoInt [20] modifies the architecture of the NeRF so that inference requires fewer samples but produces lower quality results. None of these approaches achieve real-time. The concurrent work DoNeRF adds a depth classifier to NeRF in order to drastically improve the efficiency of sampling, but requires ground-truth depth for training. Although not based on NeRF, recently Takikawa et al. [47] propose a method to accelerate neural SDF rendering with an octree. Note that this work does not model appearance properties. In contrast, we employ a volumetric representation that can capture photo-realistic view-dependent appearances while achieving even higher framerates.

3. Preliminaries

3.1. Neural Radiance Fields

Neural radiance fields (NeRF) [28] are 3D representations that can be rendered from arbitrary novel viewpoints while capturing continuous geometry and view-dependent

appearance. The radiance field is encoded into the weights of a multilayer perceptron (MLP) that can be queried at a position $\mathbf{x} = (x, y, z)$ from a viewing direction $\mathbf{d} = (\theta, \phi)$ to recover the corresponding density σ and color $c = (r, g, b)$. A pixel’s predicted color $C(\mathbf{r})$ is computed by casting a ray, \mathbf{r} , into the volume and accumulating the color based on density along the ray. NeRF estimates the accumulated color by taking N point samples along the ray to perform volume rendering:

$$\hat{C}(\mathbf{r}) = \sum_{i=0}^{N-1} T_i (1 - \exp(-\sigma_i \delta_i)) c_i, \quad (1)$$

$$\text{where } T_i = \exp \left(-\sum_{j=0}^{i-1} \sigma_j \delta_j \right) \quad (2)$$

Where δ_i are the distances between point samples. To train the NeRF network, the predicted colors \hat{C} for a batch of rays \mathcal{R} corresponding to pixels in the training images are optimized using Adam [13] to match the target pixel colors:

$$\mathcal{L}_{\text{RGB}} = \sum_{\mathbf{r} \in \mathcal{R}} \|C(\mathbf{r}) - \hat{C}(\mathbf{r})\|_2^2 \quad (3)$$

To better represent high frequency details in the scene, positional encoding is applied to the inputs, and two stages of sampling are performed. We refer the interested reader to the NeRF paper [28] paper for details.

Limitations. One notable consequence of this architecture is that each sample along the ray must be fed to the MLP to obtain the corresponding σ_i and c_i . A total of 192 samples were taken for each ray in the examples presented in NeRF. This is inefficient as most samples are sampling free space which do not contribute to the integrated color. To render a single target image at 800×800 resolution, the network must be run on over 100 million inputs. Therefore it takes about 30 seconds to render a single frame using a NVIDIA V100 GPU, making it impractical for real-time applications. Our use of a sparse voxel octree avoids excess compute in regions without content. Additionally we precompute the values for each voxel so that network queries are not performed during inference.

4. Method

We propose a pipeline that enables real-time rendering of NeRFs. Given a trained NeRF, we can convert it into a PlenOctree, an efficient data structure that is able to represent non-Lambertian effects in a scene. Specifically, it is an octree which stores spherical harmonics (SH) coefficients at the leaves, encoding view-dependent radiance.

To make the conversion to PlenOctree more straightforward, we also propose *NeRF-SH*, a variant of the NeRF net-

work which directly outputs the SH coefficients, thus eliminating the need for a view-direction input to the network. With this change, the conversion can then be performed by evaluating on a uniform grid followed by thresholding. We fine-tune the octree on the training images to further improve image quality. Please see Fig. 2 for a graphical illustration of our pipeline.

The conversion process leverages the continuous nature of NeRF to dynamically obtain the spatial structure of the octree. We show that even with a partially trained NeRF, our PlenOctree is capable of producing results competitive with the fully trained NeRF.

4.1. NeRF-SH: NeRF with Spherical Harmonics

SHs have been a popular low-dimensional representation for spherical functions and have been used to model Lambertian surfaces [34, 2] or even glossy surfaces [43]. Here we explore its use in a volumetric context. Specifically, we adapt the NeRF network f to output spherical harmonics coefficients \mathbf{k} , rather than RGB values.

$$f(\mathbf{x}) = (\mathbf{k}, \sigma) \quad \text{where } \mathbf{k} = (k_\ell^m)_{\ell:0 \leq \ell \leq \ell_{\max}}^{m: -\ell \leq m \leq \ell} \quad (4)$$

Each $k_\ell^m \in \mathbb{R}^3$ is a set of 3 coefficients corresponding to the RGB components. In this setup, the view-dependent color \mathbf{c} at a point \mathbf{x} may be determined by querying the SH functions $Y_\ell^m : \mathbb{S}^2 \mapsto \mathbb{R}$ at the desired viewing angle \mathbf{d} :

$$c(\mathbf{d}; \mathbf{k}) = S \left(\sum_{\ell=0}^{\ell_{\max}} \sum_{m=-\ell}^{\ell} k_\ell^m Y_\ell^m(\mathbf{d}) \right) \quad (5)$$

Where $S : x \mapsto (1 + \exp(-x))^{-1}$ is the sigmoid function for normalizing the colors. In other words, we factorize the view-dependent appearance with the SH basis, eliminating the view-direction input to the network and removing the need to sample view directions at conversion time. Please see the appendix for more technical discussion of SHs. With a single evaluation of the network, we can now efficiently query colors from arbitrary viewing angles at inference time. In Fig. 7, it can be seen that NeRF-SH training speed is similar to, but slightly faster than, NeRF (by about 10%).

Note that we can also project a trained NeRF to SHs directly at each point by sampling NeRF at random directions and multiplying by the SH component values to form Monte Carlo estimates of the inner products. However, this sampling process takes several hours to achieve reasonable quality and imposes a quality loss of about 2 dB.¹ Nevertheless, this alternative approach offers a pathway to convert existing NeRFs into PlenOctrees.

Other than SHs, we also experiment with Spherical Gaussians (SG) [8], a learnable spherical basis which have

¹With 10000 view-direction samples per point, taking about 2 hours, the PSNR is 29.21 vs. 31.02 for our main method prior to optimization.

Synthetic NeRF Dataset	best	second-best		
	PSNR \uparrow	SSIM \uparrow	LPIPS \downarrow	FPS \uparrow
NeRF (original)	31.01	0.947	0.081	0.023
NeRF	31.69	0.953	0.068	0.045
SRN	22.26	0.846	0.170	0.909
Neural Volumes	26.05	0.893	0.160	3.330
NSVF	31.75	0.953	0.047	0.815
AutoInt (8 sections)	25.55	0.911	0.170	0.380
NeRF-SH	31.57	0.952	0.063	0.051
PlenOctree from NeRF-SH	31.02	0.951	0.066	167.68
PlenOctree after fine-tuning	31.71	0.958	0.053	167.68

Table 1: **Quantitative results on the NeRF-synthetic test scenes.** Our approach is significantly faster than all existing methods during inference while performing on par with *NSVF*, the current state-of-the-art method for image quality. We note that *NeRF-SH*, the modified NeRF model that is trained to output SH, performs similarly to the baseline *NeRF* model. The octree conversion of *NeRF-SH* to *PlenOctree w/o fine-tuning* negatively impacts the image quality metrics. This is remedied with the additional fine-tuning step.

been used to represent all-frequency lighting [51, 43, 19]. We find that SHs perform better in our use case and provide an ablation in the appendix.

Sparsity prior. Without any regularization, the model is free to generate arbitrary geometry in unobserved regions. While this does not directly worsen image quality, it would adversely impact our conversion process as the extra geometry occupies significant voxel space.

To solve this problem, we introduce an additional sparsity prior during NeRF training. Intuitively, this prior encourages NeRF to choose empty space when both space and solid colors are possible solutions. Formally,

$$\mathcal{L}_{\text{sparsity}} = \frac{1}{K} \sum_{k=1}^K |1 - \exp(-\lambda\sigma_k)| \quad (6)$$

Here, $\{\sigma_k\}_{k=1}^K$ are the evaluated density values at K uniformly random points within the bounding box, and λ is a hyperparameter. The final training loss is then $\beta_{\text{sparsity}}\mathcal{L}_{\text{sparsity}} + \mathcal{L}_{\text{RGB}}$, where β_{sparsity} is a hyperparameter. Fig. 3 illustrates the effect of the prior.

4.2. PlenOctree: Octree-based Radiance Fields

Once we have trained a NeRF-SH model, we can convert it into a sparse octree representation for real time rendering. A PlenOctree stores density and SH coefficients modelling view-dependent appearance at each leaf. We describe the conversion and rendering processes below.

Rendering. To render the PlenOctree, for each ray, we first determine ray-voxel intersections in the octree structure. This produces a sequence of distances between voxel boundaries $\{\delta_i\}_{i=1}^N$, each of which has constant density and color. NeRF’s volume rendering model (1) is then applied to

Tanks and Temples Dataset	best	second-best		
	PSNR \uparrow	SSIM \uparrow	LPIPS \downarrow	FPS \uparrow
NeRF (original)	25.78	0.864	0.198	0.007
NeRF	27.94	0.904	0.168	0.013
SRN	24.10	0.847	0.251	0.250
Neural Volumes	23.70	0.834	0.260	1.000
NSVF	28.40	0.900	0.153	0.163
NeRF-SH	27.82	0.902	0.167	0.015
PlenOctree from NeRF-SH	27.34	0.897	0.170	42.22
PlenOctree after fine-tuning	27.99	0.917	0.131	42.22

Table 2: **Quantitative results on the Tanks and Temples test scenes.** We find that our fine-tuned *PlenOctree* model is significantly faster than existing methods while performing on par in terms of image metrics. Note that the images here are 1920×1080 compared to 800×800 in the synthetic dataset.

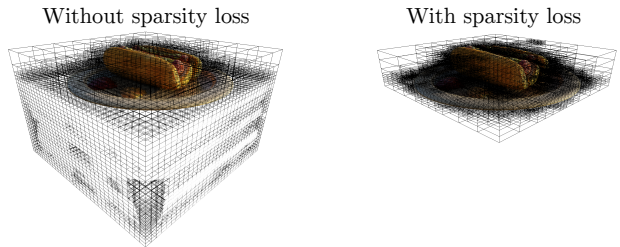


Figure 3: **Sparsity loss and conversion robustness.** When trained without the sparsity loss, NeRF can often converge to a solution where unobserved portions or the background are solid. This degrades the spatial resolution of our octree-based representation.

assign a color to the ray. Note that compared to the uniform sampling employed Neural Volumes [22], this approach is able to skip large voxels in one step while also not missing small voxels.

At test-time, we further accelerate this rendering process by applying early-stopping when the ray has accumulated transmittance T_i less than $\gamma = 0.01$.

Conversion from NeRF-SH. The conversion process can be divided into three steps. At a high level, we evaluate the network on a grid, retaining only density values, then filter the voxels via thresholding. Finally we sample random points within each remaining voxel and average them to obtain SH coefficients to store in the octree leaves. More details are given below:

Evaluation. We first evaluate the NeRF-SH model to obtain σ values on a uniformly spaced 3D grid. The grid is automatically scaled to tightly fit the scene content.²

Filtering. Next, we filter this grid to obtain a sparse set of voxels centered at the grid points sufficient for representing the scene. Specifically, we render alpha maps for all the training views using this voxel grid, keeping track of the maximum ray weight $1 - \exp(-\sigma_i \delta_i)$ at each voxel. We

²By pre-evaluating σ on a larger grid and finding the bounding box of all points with $\sigma \geq \tau_a$.

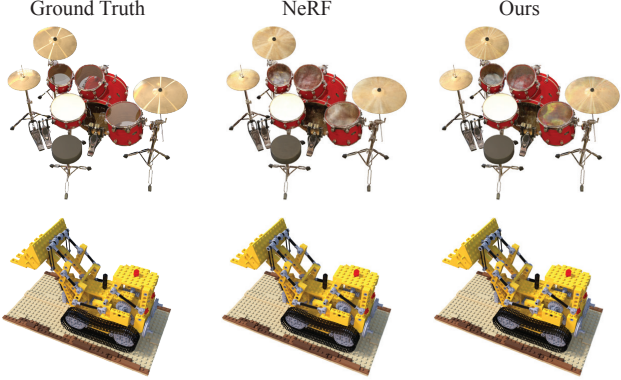


Figure 4: **NeRF-synthetic qualitative results.** Randomly sampled qualitative comparisons on a reimplementation of NeRF and our proposed method. We are unable to find any significant image quality difference between the two methods. Despite this, our method can render these examples images more than 3500x faster.

then eliminate the voxels whose weights are lower than a threshold τ_w . The octree is constructed to contain the remaining voxels as leaves at the deepest level while being empty elsewhere. Compared to naively thresholding by σ at each point, this method can eliminates non-visible voxels.

Sampling. Finally, we sample a set of 256 random points in each remaining voxel and set the associated leaf of the octree to the mean of these values to reduce aliasing. Each leaf now contains the density σ and a vector of spherical harmonics coefficients for each of the RGB color channels.

This full extraction process takes about 15 minutes.³

4.3. PlenOctree Optimization

Since this volume rendering process is fully differentiable with respect to the tree values, we can directly fine-tune the resulting octree on the original training images using the NeRF loss (3) with SGD in order to improve the image quality. Note that the tree structure is fixed to that obtained from NeRF in this process. PlenOctree optimization operates at about 3 million rays per second, compared to about 9000 for NeRF training, allowing us to optimize for many epochs in a relatively short time. The analytic derivatives for this process are implemented in custom CUDA kernels. We defer technical details to the appendix.

The fast octree optimization indirectly allows us to accelerate NeRF training, as seen in Fig. 7, since we can elect to stop the NeRF-SH training at an earlier time for constructing the PlenOctree, with only a slight degradation in quality.

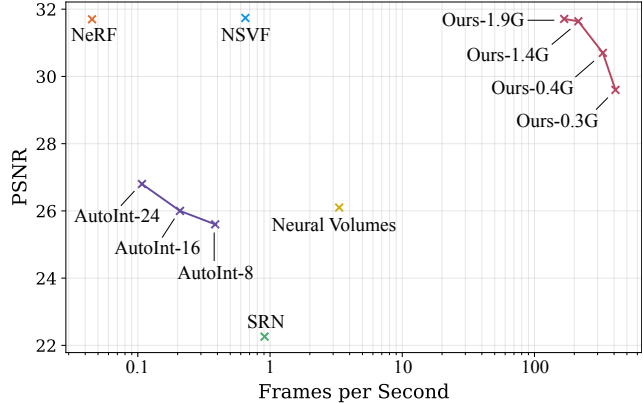


Figure 5: **Quality vs. speed comparison of various methods.** A comparison of methods on the NeRF-synthetic dataset where higher PSNR and lower FPS (top right) is most desirable. We include four variants of the PlenOctree model that tune parts of the conversion process to trade off accuracy for speed. Please see Table 3 (adjacent) for descriptions of these variants. Note that the time axis is logarithmic.

Model Description		GB ↓	PSNR ↑	FPS ↑
Ours-1.9G	Complete Model as in Table 1	1.93	31.71	168
Ours-1.4G	Higher Threshold $\tau_w = 0.01$	1.36	31.64	215
Ours-0.4G	w/o Auto Bbox Scaling	0.44	30.70	329
Ours-0.3G	Grid Size 256	0.30	29.60	410

Table 3: **PlenOctree conversion ablations on NeRF-synthetic.** Average metrics across the NeRF-synthetic scenes for several different methods to construct PlenOctrees are shown. *Ours-1.9G*: This is the high-quality model we reported in Table 1. *Ours-1.4G*: This is a variant with a higher weight threshold, therefore aggressively sparsifying the tree. *Ours-0.4G*: Here, we remove the auto bounding box scaling step and instead use fixed large bounding boxes, limiting resolution. *Ours-0.3G*: A version using a 256^3 grid instead of 512^3 .

5. Results

5.1. Experimental Setup

Datasets. For our experiments, we use the *NeRF-synthetic* [28] dataset and a subset of the *Tanks and Temples* dataset [14]. The NeRF-synthetic dataset consists of 8 scenes where each scene has a central object that is imaged with 100 inward facing cameras distributed randomly on the upper hemisphere. The images are 800×800 with provided ground truth camera poses. The Tanks and Temples subset is from NSVF [21] and contains 5 scenes of real objects captured by an inward facing camera that circles the scene. We use foreground masks provided by the NSVF authors. Each scene contains between 152-384 images of size

³Note that sampling 8 points instead of 256 allows for extraction in about 1.5 minutes, with minimal loss in quality.



Figure 6: **Qualitative comparisons on Tanks and Temples.** We compare NeRF and our proposed method. On this dataset, we find that our method better recovers the fine details in the scene. The results are otherwise similar. Additionally, the render time of our method is over 3000x faster.

1920 × 1080.

Baselines. The principal baseline for our experiments is NeRF [28]; we report results for both the original NeRF implementation, denoted *NeRF (original)* as well as a reimplementation in Jax [6], denoted simply *NeRF*, which our NeRF-SH code is based off of. Unless otherwise stated, all *NeRF* results and timings are from the latter implementation. We compare also to two recent papers introducing NeRF accelerations, neural sparse voxel fields (NSVF) [21] and AutoInt [20], as well as two older methods, scene representation networks (SRN) [42] and Neural Volumes [22].

5.2. Quality Evaluation

We evaluate our approach against prior works on the synthetic and real datasets mentioned above. The results are in Tables 1 and Table 2 respectively. Note that none of the baselines achieve real-time performance; nevertheless, our quality results are competitive in all cases and better in terms of some metrics.

In Figures 4 and 6, we show qualitative examples that demonstrate that our PlenOctree conversion does not perceptually worsen the rendered images compared to NeRF; rather, we observe that the PlenOctree optimization process *enhances* fine details such as text. Additionally, we note that our modifications of NeRF to predict spherical function coefficients (NeRF-SH) does not significantly change the performance.

For the SH, we set $\ell_{\max} = 3$ (16 components) and 4 (25 components) on the synthetic and Tanks & Temples datasets respectively. We use 512^3 grid size in either case. Please refer to the appendix for training details. The inference time performance is measured on a Tesla V100 for all methods. Across both datasets we find that PlenOctrees perform inference over 3000 times faster than NeRF and at least 30 times faster than all other compared methods. *PlenOctree*

performs either best, or second best for all image quality metrics.

5.3. Speed Trade-off Analysis

A number of parameters for PlenOctree conversion and rendering can be tuned to trade-off between speed and image quality. In Figure 5 and Table 3 we compared image accuracy and inference time for four variants of PlenOctree that sweep this trade-off.

5.4. Indirect Acceleration of NeRF Training

Since we can efficiently fine-tune the octree on the original training data, as briefly discussed in §4.3, we can choose to stop the NeRF-SH training at an earlier time before converting it to a PlenOctree. Indeed, we have found that the image quality improvements gained during fine-tuning can often be greater than continuing to train the NeRF-SH an equivalent amount of time. Therefore it can be more time efficient to stop the NeRF-SH training before it has converged and transition to PlenOctree conversion and fine-tuning.

In Figure 7 we compare NeRF and NeRF-SH models trained for 2 million iterations each to a sequence of PlenOctree models extracted from NeRF-SH checkpoints. We find that given a time constraint, it is almost always preferable to stop the NeRF training and transition to PlenOctree optimization.

5.5. Real-time and In-browser Applications

Interactive demos. Within our desktop viewer, we are able to perform a variety of real-time scene operations on the PlenOctree representation. For example, it is possible to insert meshes while maintaining proper occlusion, slice the PlenOctree to visualize a cross-section, or render the depth map to verify the geometry. Other features include probing

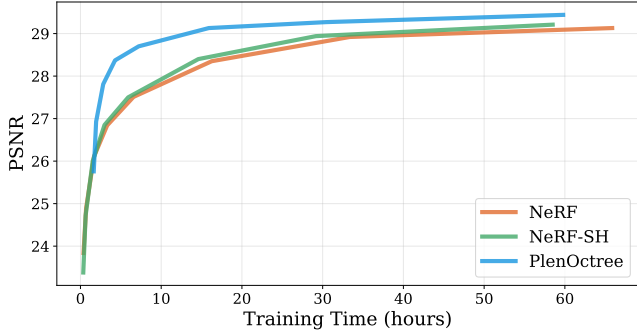


Figure 7: **Indirect training acceleration.** Training curves for fitting the synthetic NeRF *ship* scene for 2 million iterations. The baseline NeRF model and our NeRF-SH model perform similarly during training. We find that by optimizing the PlenOctree converted from NeRF-SH checkpoints, we are able to reach a similar quality more quickly. The PlenOctree conversion and fine-tuning adds approximately 1 hour to the training time; despite this, we find that it takes \sim 16 hours of NeRF training to match the same quality as the PlenOctree model after \sim 4.5 hours.



Figure 8: **Qualitative results on further real scenes.** We apply *FastNeRF* to the NeRF-360-real and LLFF datasets. While our method is not designed for unbounded or forward-facing scenes (where MPIS can be more appropriate), it nevertheless performs reasonably well. Note for forward-facing scenes, we construct the octree in NDC coordinates.

the radiance distribution at any point in space, and inspecting subsets of SH components. These examples are demonstrated in Figure 9. The ability to perform these actions in real-time is beneficial both for interactive entertainment and debugging NeRF-related applications.

Web renderer. We have implemented a web-based renderer enabling interactive viewing of converted PlenOctrees in the browser. This is achieved by rewriting our CUDA-based PlenOctree renderer as a WebGL-compatible fragment shader. We apply compressions to make serving the octrees more manageable. Please see the appendix for more information.

6. Discussion

We have introduced a new data representation for NeRFs using PlenOctrees, which enables real-time rendering capabilities for arbitrary objects and scenes. Not only can we accelerate the rendering performance of the original NeRF

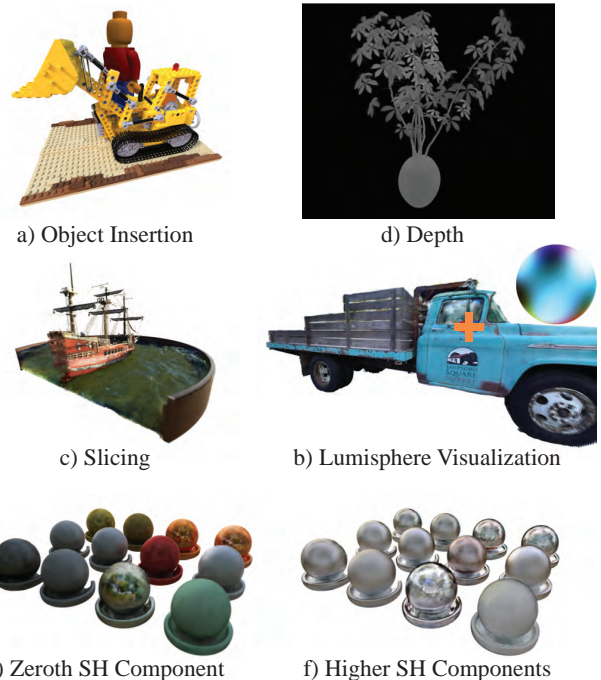


Figure 9: **Real-time interactive demos.** Set of real-time operations that can be performed on PlenOctree within our interactive viewer. This application will be released to the public.

method by more than 3000 times, but we can produce images that are either equal or better quality than NeRF thanks to our hierarchical data structure. As training time poses another hurdle for adopting NeRFs in practice (taking 1-2 days to fully converge), we also showed that our PlenOctrees can accelerate effective training time for our NeRF-SH. Finally, we have implemented an in-browser viewer based on WebGL to demonstrate real-time and 6-DOF rendering capabilities of NeRFs on consumer laptops. In the future, our approach may enable virtual online stores in VR, where any products with arbitrary complexity and materials can be visualized in real-time while enabling 6-DOF viewing.

Limitations and Future Work. While we achieve state-of-the-art rendering performance and frame rates, the octree representation is much larger than the compact representation of the original NeRF model and has a larger memory footprint. The average uncompressed octree size for the full model is 1.93 GB on the synthetic dataset and 3.53 GB on the Tanks and Temples dataset. For online delivery, we use lower-resolution compressed models which are about 30-120 MB; please see the appendix for details. Although already possible in some form (Fig. 8), applying our method to unbounded and forward-facing scenes optimally requires further work as the data distribution is different for unbounded scenes. The forward-facing scenes inherently

do not support 6-DOF viewing, and we suggest MPIS may be more appropriate in this case [56].

In the future, we plan to explore extensions of our method to enable real-time 6-DOF immersive viewing of large-scale scenes, as well as of dynamic scenes. We believe that real-time rendering of NeRFs has the potential to become a new standard for next-generation AR/VR technologies, as photorealistic 3D content can be digitized as easily as recording 2D videos.

References

- [1] Edward H Adelson, James R Bergen, et al. *The plenoptic function and the elements of early vision*, volume 2. Vision and Modeling Group, Media Laboratory, Massachusetts Institute of . . ., 1991. 2
- [2] Ronen Basri and David W Jacobs. Lambertian reflectance and linear subspaces. *IEEE transactions on pattern analysis and machine intelligence*, 25(2):218–233, 2003. 4
- [3] Chris Buehler, Michael Bosse, Leonard McMillan, Steven Gortler, and Michael Cohen. Unstructured lumigraph rendering. In *Proceedings of the 28th annual conference on Computer graphics and interactive techniques*, pages 425–432, 2001. 2
- [4] Zhiqin Chen and Hao Zhang. Learning implicit fields for generative shape modeling. In *IEEE Computer Vision and Pattern Recognition (CVPR)*, 2019. 3
- [5] Paul E Debevec, Camillo J Taylor, and Jitendra Malik. Modeling and rendering architecture from photographs: A hybrid geometry-and image-based approach. In *Proceedings of the 23rd annual conference on Computer graphics and interactive techniques*, pages 11–20, 1996. 2
- [6] Boyang Deng, Jonathan T. Barron, and Pratul P. Srinivasan. JaxNeRF: an efficient JAX implementation of NeRF, 2020. 7, 14
- [7] Robert A Drebin, Loren Carpenter, and Pat Hanrahan. Volume rendering. *ACM Siggraph Computer Graphics*, 22(4):65–74, 1988. 2
- [8] Ronald Aylmer Fisher. Dispersion on a sphere. *Proceedings of the Royal Society of London. Series A. Mathematical and Physical Sciences*, 217(1130):295–305, 1953. 4, 11, 12
- [9] Amos Gropp, Lior Yariv, Niv Haim, Matan Atzmon, and Yaron Lipman. Implicit geometric regularization for learning shapes. *ICML*, 2020. 3
- [10] Christian Häne, Shubham Tulsiani, and Jitendra Malik. Hierarchical surface prediction for 3d object reconstruction. In *2017 International Conference on 3D Vision (3DV)*, pages 412–420. IEEE, 2017. 3
- [11] Paul Heckbert. Color image quantization for frame buffer display. *ACM SIGGRAPH Proceedings*, 1982. 12
- [12] Abhishek Kar, Christian Häne, and Jitendra Malik. Learning a multi-view stereo machine. *arXiv preprint arXiv:1708.05375*, 2017. 2
- [13] Diederik P Kingma and Jimmy Ba. Adam: A method for stochastic optimization. *arXiv preprint arXiv:1412.6980*, 2014. 4, 14
- [14] Arno Knapitsch, Jaesik Park, Qian-Yi Zhou, and Vladlen Koltun. Tanks and temples: Benchmarking large-scale scene reconstruction. *ACM Transactions on Graphics (ToG)*, 36(4):1–13, 2017. 6
- [15] Aaron Knoll. A survey of octree volume rendering methods. *GI, the Gesellschaft für Informatik*, page 87, 2006. 3
- [16] Kiriakos N Kutulakos and Steven M Seitz. A theory of shape by space carving. *International journal of computer vision*, 38(3):199–218, 2000. 2
- [17] Marc Levoy and Pat Hanrahan. Light field rendering. In *Proceedings of the 23rd annual conference on Computer graphics and interactive techniques*, pages 31–42, 1996. 2
- [18] Rui long Li, Yuliang Xiu, Shunsuke Saito, Zeng Huang, Kyle Olszewski, and Hao Li. Monocular real-time volumetric performance capture. In *European Conference on Computer Vision*, pages 49–67. Springer, 2020. 3
- [19] Zhengqin Li, Mohammad Shafiei, Ravi Ramamoorthi, Kalyan Sunkavalli, and Manmohan Chandraker. Inverse rendering for complex indoor scenes: Shape, spatially-varying lighting and svbrdf from a single image. In *Proceedings of the IEEE/CVF Conference on Computer Vision and Pattern Recognition*, pages 2475–2484, 2020. 5, 12
- [20] David B Lindell, Julien NP Martel, and Gordon Wetzstein. Autoint: Automatic integration for fast neural volume rendering. *arXiv preprint arXiv:2012.01714*, 2020. 3, 7
- [21] Lingjie Liu, Jiatao Gu, Kyaw Zaw Lin, Tat-Seng Chua, and Christian Theobalt. Neural sparse voxel fields. *NeurIPS*, 2020. 3, 6, 7, 11
- [22] Stephen Lombardi, Tomas Simon, Jason Saragih, Gabriel Schwartz, Andreas Lehrmann, and Yaser Sheikh. Neural volumes: Learning dynamic renderable volumes from images. *ACM Trans. Graph.*, 38(4):65:1–65:14, July 2019. 1, 2, 5, 7, 11
- [23] Stephen Lombardi, Tomas Simon, Gabriel Schwartz, Michael Zollhoefer, Yaser Sheikh, and Jason Saragih. Mixture of volumetric primitives for efficient neural rendering, 2021. preprint. 3
- [24] Jean loup Gailly and Mark Adler. zlib, 2017. 12
- [25] Ricardo Martin-Brualla, Noha Radwan, Mehdi S. M. Sajjadi, Jonathan T. Barron, Alexey Dosovitskiy, and Daniel Duckworth. NeRF in the Wild: Neural Radiance Fields for Unconstrained Photo Collections. In *CVPR*, 2021. 3
- [26] Lars Mescheder, Michael Oechsle, Michael Niemeyer, Sebastian Nowozin, and Andreas Geiger. Occupancy networks: Learning 3d reconstruction in function space. In *Proceedings IEEE Conf. on Computer Vision and Pattern Recognition (CVPR)*, 2019. 3
- [27] Ben Mildenhall, Pratul P Srinivasan, Rodrigo Ortiz-Cayon, Nima Khademi Kalantari, Ravi Ramamoorthi, Ren Ng, and Abhishek Kar. Local light field fusion: Practical view synthesis with prescriptive sampling guidelines. *ACM Transactions on Graphics (TOG)*, 38(4):1–14, 2019. 2
- [28] Ben Mildenhall, Pratul P. Srinivasan, Matthew Tancik, Jonathan T. Barron, Ravi Ramamoorthi, and Ren Ng. NeRF: Representing scenes as neural radiance fields for view synthesis. *ECCV*, 2020. 1, 3, 4, 6, 7

[29] Michael Niemeyer, Lars Mescheder, Michael Oechsle, and Andreas Geiger. Differentiable volumetric rendering: Learning implicit 3d representations without 3d supervision. In *Proc. IEEE Conf. on Computer Vision and Pattern Recognition (CVPR)*, 2020. 3

[30] Jeong Joon Park, Peter Florence, Julian Straub, Richard Newcombe, and Steven Lovegrove. Deep sdf: Learning continuous signed distance functions for shape representation. In *The IEEE Conference on Computer Vision and Pattern Recognition (CVPR)*, June 2019. 3

[31] Keunhong Park, Utkarsh Sinha, Jonathan T Barron, Sofien Bouaziz, Dan B Goldman, Steven M Seitz, and Ricardo-Martin Brualla. Deformable neural radiance fields. *arXiv preprint arXiv:2011.12948*, 2020. 3

[32] Songyou Peng, Michael Niemeyer, Lars Mescheder, Marc Pollefeys, and Andreas Geiger. Convolutional occupancy networks. In *European Conference on Computer Vision (ECCV)*, 2020. 3

[33] Eric Penner and Li Zhang. Soft 3d reconstruction for view synthesis. *ACM Transactions on Graphics (TOG)*, 36(6):1–11, 2017. 2

[34] Ravi Ramamoorthi and Pat Hanrahan. On the relationship between radiance and irradiance: determining the illumination from images of a convex lambertian object. *JOSA A*, 18(10):2448–2459, 2001. 4

[35] Daniel Rebain, Wei Jiang, Soroosh Yazdani, Ke Li, Kwang Moo Yi, and Andrea Tagliasacchi. Derf: Decomposed radiance fields. *arXiv preprint arXiv:2011.12490*, 2020. 3

[36] Gernot Riegler, Ali Osman Ulusoy, and Andreas Geiger. Octnet: Learning deep 3d representations at high resolutions. In *Proceedings of the IEEE Conference on Computer Vision and Pattern Recognition*, 2017. 3

[37] Shunsuke Saito, Zeng Huang, Ryota Natsume, Shigeo Morishima, Angjoo Kanazawa, and Hao Li. Pifu: Pixel-aligned implicit function for high-resolution clothed human digitization. In *The IEEE International Conference on Computer Vision (ICCV)*, October 2019. 3

[38] Katja Schwarz, Yiyi Liao, Michael Niemeyer, and Andreas Geiger. Graf: Generative radiance fields for 3d-aware image synthesis. *arXiv preprint arXiv:2007.02442*, 2020. 3

[39] Steven M Seitz and Charles R Dyer. Photorealistic scene reconstruction by voxel coloring. *International Journal of Computer Vision*, 35(2):151–173, 1999. 2

[40] Jonathan Shade, Steven Gortler, Li-wei He, and Richard Szeliski. Layered depth images. In *Proceedings of the 25th annual conference on Computer graphics and interactive techniques*, pages 231–242, 1998. 2

[41] Vincent Sitzmann, Justus Thies, Felix Heide, Matthias Nießner, Gordon Wetzstein, and Michael Zollhofer. Deepvoxels: Learning persistent 3d feature embeddings. In *Proceedings of the IEEE/CVF Conference on Computer Vision and Pattern Recognition*, pages 2437–2446, 2019. 2

[42] Vincent Sitzmann, Michael Zollhöfer, and Gordon Wetzstein. Scene representation networks: Continuous 3d-structure-aware neural scene representations. *arXiv preprint arXiv:1906.01618*, 2019. 3, 7, 11

[43] Peter-Pike Sloan, Jan Kautz, and John Snyder. Precomputed radiance transfer for real-time rendering in dynamic, low-frequency lighting environments. In *Proceedings of the 29th annual conference on Computer graphics and interactive techniques*, pages 527–536, 2002. 4, 5, 12

[44] Pratul P Srinivasan, Boyang Deng, Xiuming Zhang, Matthew Tancik, Ben Mildenhall, and Jonathan T Barron. Nerv: Neural reflectance and visibility fields for relighting and view synthesis. *arXiv preprint arXiv:2012.03927*, 2020. 3

[45] Pratul P Srinivasan, Richard Tucker, Jonathan T Barron, Ravi Ramamoorthi, Ren Ng, and Noah Snavely. Pushing the boundaries of view extrapolation with multiplane images. In *Proceedings of the IEEE/CVF Conference on Computer Vision and Pattern Recognition*, pages 175–184, 2019. 2

[46] Richard Szeliski and Polina Golland. Stereo matching with transparency and matting. In *Sixth International Conference on Computer Vision (IEEE Cat. No. 98CH36271)*, pages 517–524. IEEE, 1998. 2

[47] Towaki Takikawa, Joey Litalien, Kangxue Yin, Karsten Kreis, Charles Loop, Derek Nowrouzezahrai, Alec Jacobson, Morgan McGuire, and Sanja Fidler. Neural geometric level of detail: Real-time rendering with implicit 3D shapes. *arXiv preprint arXiv:2101.10994*, 2021. 3

[48] Matthew Tancik, Ben Mildenhall, Terrance Wang, Divi Schmidt, Pratul P. Srinivasan, Jonathan T. Barron, and Ren Ng. Learned initializations for optimizing coordinate-based neural representations. In *CVPR*, 2021. 3

[49] Maxim Tatarchenko, Alexey Dosovitskiy, and Thomas Brox. Octree generating networks: Efficient convolutional architectures for high-resolution 3d outputs. In *Proceedings of the IEEE International Conference on Computer Vision*, pages 2088–2096, 2017. 3

[50] Alex Trevithick and Bo Yang. Grf: Learning a general radiance field for 3d scene representation and rendering. *arXiv preprint arXiv:2010.04595*, 2020. 3

[51] Yu-Ting Tsai and Zen-Chung Shih. All-frequency precomputed radiance transfer using spherical radial basis functions and clustered tensor approximation. *ACM Transactions on graphics (TOG)*, 25(3):967–976, 2006. 5, 12

[52] Shubham Tulsiani, Tinghui Zhou, Alexei A Efros, and Jitendra Malik. Multi-view supervision for single-view reconstruction via differentiable ray consistency. In *Proceedings of the IEEE conference on computer vision and pattern recognition*, pages 2626–2634, 2017. 2

[53] Michael Waechter, Nils Moehrle, and Michael Goesele. Let there be color! large-scale texturing of 3d reconstructions. In *ECCV*, pages 836–850. Springer, 2014. 2

[54] Peng-Shuai Wang, Yang Liu, Yu-Xiao Guo, Chun-Yu Sun, and Xin Tong. O-cnn: Octree-based convolutional neural networks for 3d shape analysis. *ACM Transactions on Graphics (TOG)*, 36(4):1–11, 2017. 3

[55] Qianqian Wang, Zhicheng Wang, Kyle Genova, Pratul Srinivasan, Howard Zhou, Jonathan T Barron, Ricardo Martin-Brualla, Noah Snavely, and Thomas Funkhouser. Ibrnet: Learning multi-view image-based rendering. *arXiv preprint arXiv:2102.13090*, 2021. 3

[56] Suttisak Wizadwongs, Pakkapon Phongthawee, Jiraphon Yenphraphai, and Supasorn Suwajanakorn. *Nex: Real-time view synthesis with neural basis expansion*. 2021. 3, 9

[57] Daniel N Wood, Daniel I Azuma, Ken Aldinger, Brian Curless, Tom Duchamp, David H Salesin, and Werner Stuetzle. Surface light fields for 3d photography. In *Proceedings of the 27th annual conference on Computer graphics and interactive techniques*, pages 287–296, 2000. 2

[58] Qiangeng Xu, Weiyue Wang, Duygu Ceylan, Radomir Mech, and Ulrich Neumann. *Disn: Deep implicit surface network for high-quality single-view 3d reconstruction*. In H. Wallach, H. Larochelle, A. Beygelzimer, F. d’Alché-Buc, E. Fox, and R. Garnett, editors, *Advances in Neural Information Processing Systems 32*, pages 492–502. Curran Associates, Inc., 2019. 3

[59] Lior Yariv, Yoni Kasten, Dror Moran, Meirav Galun, Matan Atzmon, Basri Ronen, and Yaron Lipman. Multiview neural surface reconstruction by disentangling geometry and appearance. *Advances in Neural Information Processing Systems*, 33, 2020. 3

[60] Alex Yu, Vickie Ye, Matthew Tancik, and Angjoo Kanazawa. *pixelnerf: Neural radiance fields from one or few images*. In *CVPR*, 2021. 3

[61] Tinghui Zhou, Richard Tucker, John Flynn, Graham Fyffe, and Noah Snavely. *Stereo magnification: Learning view synthesis using multiplane images*. *arXiv preprint arXiv:1805.09817*, 2018. 2

Appendix

A. Additional Results

A.1. Detailed comparisons

Here we provide further qualitative comparisons with baselines: SRN [42], Neural Volumes [22], NSVF [21] in Figure 10. We show more qualitative results of our method in Figure 11 and Figure 12. We also report a per-scene breakdown of the quantitative metrics against all approaches in Table 5, 6, 7, 8.

A.2. Spherical Basis Function Ablation

We also provide ablation studies on the choice of spherical basis functions. We first ablate the effect on the number of spherical harmonics basis, then we explore the use of a learnable spherical basis functions. All experiments are conducted on NeRF-synthetic dataset and we report the average metric directly after training NeRF with spherical basis functions and after converting it to PlenOctrees with fine-tuning.

Number of SH basis functions First, we ablate the number of basis functions used for spherical harmonics. Average metrics across the NeRF-synthetic dataset are reported both for the modified NeRF model and the corresponding PlenOctree. We found that switching between $\ell_{\max} = 3$

Basis	NeRF-SH/SG			Converted PlenOctree				
	PSNR \uparrow	SSIM \uparrow	LPIPS \downarrow	PSNR \uparrow	SSIM \uparrow	LPIPS \downarrow	GB \downarrow	FPS \uparrow
SH-9	31.44	0.951	0.065	31.45	0.956	0.056	1.00	262
SH-16	31.57	0.952	0.063	31.71	0.958	0.053	1.93	168
SH-25	31.56	0.951	0.063	31.69	0.958	0.052	2.68	128
SG-25	31.74	0.953	0.062	31.63	0.958	0.052	2.26	151

Table 4: **Spherical Basis Function Ablation.** We experiment with various versions of spherical basis functions, including *SH-16*, *SH-25* and *SG-25*.

(*SH-16*) and 4 (*SH-25*) makes very little difference in terms of metrics or visual quality.

Spherical Gaussians Furthermore, we also experimented with spherical Gaussians (SGs) [8], which is another form of spherical basis functions similar to spherical harmonics, but with learnable Gaussian kernels. Please see §B.1 for a brief introduction of SHs and SGs. *SG-25* denotes our model using 25 SG components instead of SH, all with learnable lobe axis \mathbf{p} and bandwidth λ . However, while this model has marginally better PSNR, the advantage disappears following PlenOctree conversion and fine-tuning.

B. Technical Details

B.1. Spherical Basis Functions: SH and SG

In the main paper, we used the SH functions without defining their exact form. Here, we provide a brief technical discussion of both spherical harmonics (SH) and spherical Gaussians (SG) for completeness.

Spherical Harmonics. The Spherical Harmonics (SH) form a complete basis of functions $\mathbb{S}^2 \rightarrow \mathbb{C}$. For $\ell \in \mathbb{N} \cup \{0\}$ and $m \in \{-\ell, \dots, \ell\}$, the SH function of degree ℓ and order m is defined as:

$$Y_\ell^m(\theta, \phi) = \sqrt{\frac{2\ell+1}{4\pi} \frac{(\ell-m)!}{(\ell+m)!}} P_\ell^m(\cos \theta) e^{im\phi} \quad (7)$$

where $P_\ell^m(\cos \theta) e^{im\phi}$ are the associated Legendre polynomials. A real basis of SH $Y_\ell^m : \mathbb{S}^2 \mapsto \mathbb{R}$ can be defined in terms of its complex analogue $Y_\ell^m : \mathbb{S}^2 \mapsto \mathbb{C}$ by setting

$$Y_\ell^m(\theta, \phi) = \begin{cases} \sqrt{2}(-1)^m \operatorname{Im}[Y_\ell^{|m|}] & \text{if } m < 0 \\ Y_\ell^0 & \text{if } m = 0 \\ \sqrt{2}(-1)^m \operatorname{Re}[Y_\ell^m] & \text{if } m > 0 \end{cases} \quad (8)$$

Any real spherical function $L : \mathbb{S}^2 \rightarrow \mathbb{R}$ may then be expressed in the SH basis:

$$L(\mathbf{d}) = L(\theta, \phi) = \sum_{\ell=0}^{\infty} \sum_{m=-\ell}^{\ell} k_\ell^m Y_\ell^m(\theta, \phi) \quad (9)$$

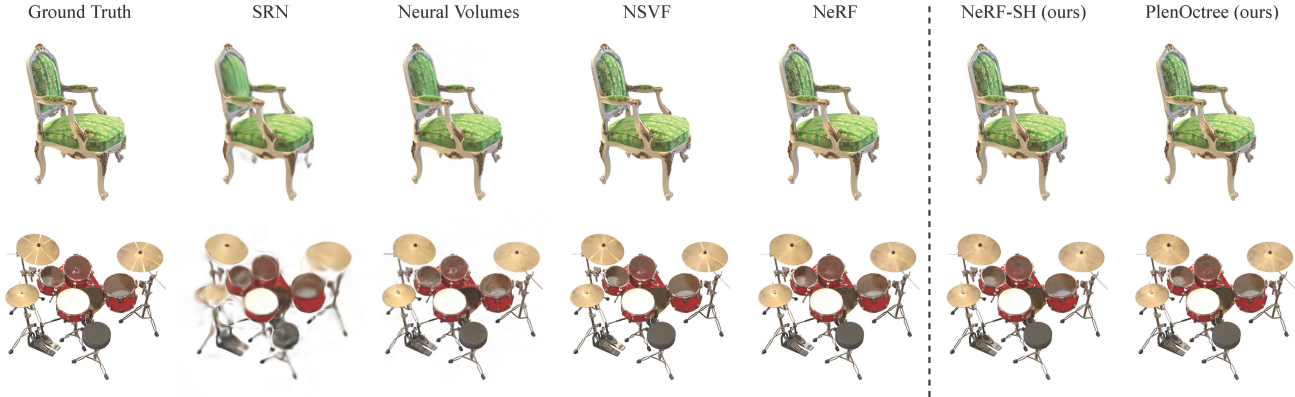


Figure 10: **Qualitative comparisons on NeRF-synthetic.**

Spherical Gaussians. Spherical Gaussians (SGs), also known as the von Mises-Fisher distribution [8], is another form of spherical basis functions that have been widely adopted to approximate spherical functions. Unlike SHs, SGs are a learnable basis. A normalized SG is defined as:

$$G(\mathbf{d}; \mathbf{p}, \lambda) = e^{\lambda(\mathbf{d} \cdot \mathbf{p} - 1)} \quad (10)$$

Where $\mathbf{p} \in \mathbb{R}^2$ is the lobe axis, and $\lambda \in \mathbb{R}$ is the bandwidth (sharpness) of the Gaussian kernel. Due to the varying bandwidths supported by SGs, they are suitable for representing all-frequency signals such as lighting [51, 43, 19]. A spherical function represented using n SGs is formulated as:

$$L(\mathbf{d}) \approx \sum_{\ell=0}^n k_{\ell} G_{\ell}(\mathbf{d}; \mathbf{p}, \lambda) \quad (11)$$

Where $k_{\ell} \in \mathbb{R}^3$ is the RGB coefficients for each SG.

B.2. PlenOctree Compression

The uncompressed PlenOctree file would be unpleasantly time-consuming for users to download for in-browser rendering. Thus, to minimize the size of PlenOctrees for viewing in the browser, we use SH-9 instead of SH-16 or SH-25 and apply a looser bounding box, which reduces the number of occupied voxels. On top of this, we compress the PlenOctrees directly in the following ways:

1. We quantize the SH coefficients in the tree using the popular median-cut algorithm [11]. More specifically, the σ values are kept as is; for each SH basis function, we quantize the RGB coefficients $k_{\ell}^m \in \mathbb{R}^3$ into 2^{16} colors. Afterwards, separately for each SH basis function, we store a $2^{16} \times 3$ codebook (as `float16`) along with pointers from each tree leaf to a position in the codebook (as `int16`).

2. We compress the entire tree, including pointers, using the standard DEFLATE algorithm from ZLIB [24].

This process reduces the file size by as much as 20-30 times. The tree is fully decompressed before it is displayed in the web renderer. We will also release this code.

B.3. Analytic Derivatives of PlenOctree Rendering

In this section, we derive the analytic derivatives of the NeRF piecewise constant volume rendering model for optimizing PlenOctrees directly. Throughout this section we will consider a fixed ray with a given origin and direction.

B.3.1 Definitions

For precision, we provide definitions of quantities used in NeRF volume rendering. The NeRF rendering model considers a ray divided into N consecutive segments with endpoints $\{t_i\}_{i=0}^N$, where t_0 and t_N are the near and far bounds. The segments have constant densities $\sigma = (\sigma_0, \dots, \sigma_{N-1})$ where each $\sigma_i \geq 0$. If we shine a light of intensity 1 at t_i , then at the camera position t_0 , the light intensity is given by

$$T_i(\sigma) := \prod_{j=0}^{i-1} \exp(-\delta_j \sigma_j), \quad (12)$$

Where $\delta_i := t_{i+1} - t_i$ are segment lengths as in §3 of the main paper. Note that T_i is also known as the accumulated transmittance from t_0 to t_i , and is the same as the definition in (1). It can be shown that this precisely models the absorption within each segment in the piecewise-constant setting.

Let $\mathbf{c} = (c_0, \dots, c_{N-1})$ be the color associated with segments $0, \dots, N-1$, and c_N be the background light intensity; each $c_0, \dots, c_N \in [0, 1]^3$ is an RGB color. We are interested in the derivative of the rendered color $\hat{C}(\sigma, \mathbf{c})$



Figure 11: **More qualitative results of our PlenOctrees on NeRF-synthetic.**



Figure 12: **More qualitative results of our PlenOctrees on Tanks&Temples.**

with respect to σ and \mathbf{c} . Note c_N (background) is typically considered a hyperparameter.

Where $w_i(\sigma) = T_i(\sigma)(1 - \exp(-\sigma_i \delta_i)) = T_i(\sigma) - T_{i+1}(\sigma)$ are segment weights, and $w_N(\sigma) = T_N(\sigma)$.⁴

B.3.2 Derivation of the Derivatives

From the original NeRF rendering equation (1), we can express the rendered ray color $\hat{C}(\sigma, \mathbf{c})$ as:

$$\hat{C}(\sigma, \mathbf{c}) = T_N(\sigma) c_N + \sum_{i=0}^{N-1} T_i(\sigma) (1 - e^{-\sigma_i \delta_i}) c_i \quad (13)$$

$$= \sum_{i=0}^N w_i(\sigma) c_i \quad (14)$$

Color derivative. Since the rendered color are a convex combination of the segment colors, it's immediately clear that

$$\frac{\partial \hat{C}}{\partial c_i}(\sigma, \mathbf{c}) = w_i(\sigma) \quad (15)$$

Handling spherical harmonics colors is straightforward by applying the chain rule, noting that the SH basis function values are constant across the ray.

⁴Note that the background color c_N was omitted in equation (1) of the main paper for simplicity.

Density derivative. This is slightly more tricky. We can write the derivative wrt. σ_i ,

$$\frac{\partial \hat{C}}{\partial \sigma_i}(\boldsymbol{\sigma}, \mathbf{c}) = c_N \frac{\partial T_N}{\partial \sigma_i} \sum_{k=0}^{N-1} c_k \left(\frac{\partial T_k}{\partial \sigma_i} - \frac{\partial T_{k+1}}{\partial \sigma_i} \right) \quad (16)$$

Where the derivative of the intensity T_k , is

$$\frac{\partial T_k}{\partial \sigma_i}(\boldsymbol{\sigma}) = \frac{\partial}{\partial \sigma_i} \left[\prod_{j=0}^{k-1} e^{-\delta_j \sigma_j} \right] \quad (17)$$

$$= -\delta_i \left[\prod_{j=0}^{k-1} e^{-\delta_j \sigma_j} \right] 1_{k>i} \quad (18)$$

$$= -\delta_i T_k(\boldsymbol{\sigma}) 1_{k>i} \quad (19)$$

$1_{k>i}$ denotes an indicator function whose value is 1 if $k > i$ or 0 else. Basically, we can delete any T_k for $k \leq i$ from the original expression, then multiply by $-\delta_i$. Therefore we can simplify (16) as follows

$$\frac{\partial \hat{C}}{\partial \sigma_i}(\boldsymbol{\sigma}, \mathbf{c}) = \delta_i \left[c_i T_{i+1}(\boldsymbol{\sigma}) - \sum_{k=i+1}^N c_k w_k(\boldsymbol{\sigma}) \right] \quad (20)$$

Remark. Within the PlenOctree renderer, this gradient can be computed in two rendering passes; the second pass is needed due to dependency on “future” weights and colors not seen by the ray marching process. The first pass store $\sum_{k=0}^N c_k w_k(\boldsymbol{\sigma})$, then subtracting a prefix from it. The overhead is still relatively small, and auxiliary memory use is constant.

If there are multiple colors, we simply add the density derivatives over all of them. In practice, usually the network outputs $\tilde{\sigma}_i \in \mathbb{R}$ and we set $\sigma_i = (\tilde{\sigma}_i)_+$, so we also need to take care of setting the gradient to 0 if $\tilde{\sigma}_i \leq 0$.

B.4. NeRF-SH Training Details

Our NeRF-SH model is built upon a Jax reimplementation of NeRF [6]. In our experiments, we use a batch size of 1024 rays, each with 64 sampled points in the coarse volume and 128 additional sampled points in the fine volume. The model is optimized with the Adam optimizer [13] using a learning rate that starts at 5×10^{-4} and decays exponentially to 5×10^{-6} over the training process. All of our models are trained for 2M iterations under the same protocol. Training takes around 50 hours to converge for each model on a single NVIDIA V100 GPU.

B.5. PlenOctree Optimization Details

After converting the NeRF-SH model into a PlenOctree, we further optimize the PlenOctree on the training set with

SGD using the NeRF loss; note we no longer apply the sparsity prior here since the octree is already sparse. For NeRF-synthetic dataset, we use a constant 1×10^7 learning rate and optimize for maximum 80 epochs. For Tanks&Temples dataset, we set the learning rate to 1.5×10^6 and the maximum epochs to 40. We applied early stopping for the optimization process by monitoring the PSNR on the validation set⁵. On average it takes around 10 minutes to finish the PlenOctree optimization for each scene on a single NVIDIA V100 GPU. The entire optimization process is performed in `float32` for stability, but afterwards we storage the PlenOctree with `float16` to reduce the model size.

⁵For Tanks&Temples dataset, we hold out 10% of the training set as validation set only for PlenOctree optimization.

PSNR \uparrow									
	Chair	Drums	Ficus	Hotdog	Lego	Materials	Mic	Ship	Mean
NeRF (original)	33.00	25.01	30.13	36.18	32.54	29.62	32.91	28.65	31.01
NeRF	34.08	25.03	30.43	36.92	33.28	29.91	34.53	29.36	31.69
SRN	26.96	17.18	20.73	26.81	20.85	18.09	26.85	20.60	22.26
Neural Volumes	28.33	22.58	24.79	30.71	26.08	24.22	27.78	23.93	26.05
NSVF	33.19	25.18	31.23	37.14	32.29	32.68	34.27	27.93	31.75
NeRF-SH	33.98	25.17	30.72	36.75	32.77	29.95	34.04	29.21	31.57
PlenOctree from NeRF-SH	33.19	25.01	30.56	36.15	32.12	29.56	33.01	28.58	31.02
PlenOctree after fine-tuning	34.66	25.31	30.79	36.79	32.95	29.76	33.97	29.42	31.71

SSIM \uparrow									
	Chair	Drums	Ficus	Hotdog	Lego	Materials	Mic	Ship	Mean
NeRF (original)	0.967	0.925	0.964	0.974	0.961	0.949	0.980	0.856	0.947
NeRF	0.975	0.925	0.967	0.979	0.968	0.952	0.987	0.868	0.953
SRN	0.910	0.766	0.849	0.923	0.809	0.808	0.947	0.757	0.846
Neural Volumes	0.916	0.873	0.910	0.944	0.880	0.888	0.946	0.784	0.893
NSVF	0.968	0.931	0.960	0.987	0.973	0.854	0.980	0.973	0.953
NeRF-SH	0.974	0.927	0.968	0.978	0.966	0.951	0.985	0.866	0.952
PlenOctree from NeRF-SH	0.970	0.927	0.968	0.977	0.965	0.953	0.983	0.863	0.951
PlenOctree after fine-tuning	0.981	0.933	0.970	0.982	0.971	0.955	0.987	0.884	0.958

LPIPS \downarrow									
	Chair	Drums	Ficus	Hotdog	Lego	Materials	Mic	Ship	Mean
NeRF (original)	0.046	0.091	0.044	0.121	0.050	0.063	0.028	0.206	0.081
NeRF	0.035	0.085	0.038	0.079	0.040	0.060	0.019	0.185	0.068
SRN	0.106	0.267	0.149	0.100	0.200	0.174	0.063	0.299	0.170
Neural Volumes	0.109	0.214	0.162	0.109	0.175	0.130	0.107	0.276	0.160
NSVF	0.043	0.069	0.017	0.025	0.029	0.021	0.010	0.162	0.047
NeRF-SH	0.037	0.087	0.039	0.041	0.041	0.060	0.021	0.177	0.063
PlenOctree from NeRF-SH	0.039	0.088	0.038	0.044	0.046	0.063	0.023	0.189	0.066
PlenOctree after fine-tuning	0.022	0.076	0.038	0.032	0.034	0.059	0.017	0.144	0.053

FPS \uparrow									
	Chair	Drums	Ficus	Hotdog	Lego	Materials	Mic	Ship	Mean
NeRF (original)	0.023	0.023	0.023	0.023	0.023	0.023	0.023	0.023	0.023
NeRF	0.045	0.045	0.045	0.045	0.045	0.045	0.045	0.045	0.045
SRN	0.909	0.909	0.909	0.909	0.909	0.909	0.909	0.909	0.909
Neural Volumes	3.330	3.330	3.330	3.330	3.330	3.330	3.330	3.330	3.330
NSVF	1.044	0.735	0.597	0.660	0.633	0.517	1.972	0.362	0.815
NeRF-SH	0.051	0.051	0.051	0.051	0.051	0.051	0.051	0.051	0.051
PlenOctree	352.4	175.9	85.6	95.5	186.8	64.2	324.9	56.0	167.7

Table 5: Per-scene quantitative results on NeRF-synthetic dataset.

PSNR \uparrow						
	Barn	Caterpillar	Family	Ignatius	Truck	Mean
NeRF (original)	24.05	23.75	30.29	25.43	25.36	25.78
NeRF	27.39	25.24	32.47	27.95	26.66	27.94
SRN	22.44	21.14	27.57	26.70	22.62	24.09
Neural Volumes	20.82	20.71	28.72	26.54	21.71	23.70
NSVF	27.16	26.44	33.58	27.91	26.92	28.40
NeRF-SH	27.05	25.06	32.28	28.06	26.66	27.82
PlenOctree from NeRF-SH	25.78	24.80	32.04	27.92	26.15	27.34
PlenOctree after fine-tuning	26.80	25.29	32.85	28.19	26.83	27.99
SSIM \uparrow						
	Barn	Caterpillar	Family	Ignatius	Truck	Mean
NeRF (original)	0.750	0.860	0.932	0.920	0.860	0.864
NeRF	0.842	0.892	0.951	0.940	0.896	0.904
SRN	0.741	0.834	0.908	0.920	0.832	0.847
Neural Volumes	0.721	0.819	0.916	0.922	0.793	0.834
NSVF	0.823	0.900	0.954	0.930	0.895	0.900
NeRF-SH	0.838	0.891	0.949	0.940	0.895	0.902
PlenOctree from NeRF-SH	0.820	0.889	0.948	0.940	0.889	0.897
PlenOctree after fine-tuning	0.856	0.907	0.962	0.948	0.914	0.917
LPIPS \downarrow						
	Barn	Caterpillar	Family	Ignatius	Truck	Mean
NeRF (original)	0.395	0.196	0.098	0.111	0.192	0.198
NeRF	0.286	0.189	0.092	0.102	0.173	0.168
SRN	0.448	0.278	0.134	0.128	0.266	0.251
Neural Volumes	0.479	0.280	0.111	0.117	0.312	0.260
NSVF	0.307	0.141	0.063	0.106	0.148	0.153
NeRF-SH	0.291	0.185	0.091	0.091	0.175	0.167
PlenOctree from NeRF-SH	0.296	0.188	0.094	0.092	0.180	0.170
PlenOctree after fine-tuning	0.226	0.148	0.069	0.080	0.130	0.131
FPS \uparrow						
	Barn	Caterpillar	Family	Ignatius	Truck	Mean
NeRF (original)	0.007	0.007	0.007	0.007	0.007	0.007
NeRF	0.013	0.013	0.013	0.013	0.013	0.013
SRN	0.250	0.250	0.250	0.250	0.250	0.250
Neural Volumes	1.000	1.000	1.000	1.000	1.000	1.000
NSVF	10.74	5.415	2.625	6.062	5.886	6.146
NeRF-SH	0.015	0.015	0.015	0.015	0.015	0.015
PlenOctree (ours)	46.94	54.00	32.33	15.67	62.16	42.22

Table 6: Per-scene quantitative results on Tanks&Temples dataset.

	PSNR \uparrow									
	Chair	Drums	Ficus	Hotdog	Lego	Materials	Mic	Ship	Mean	
Ours-1.9G	34.66	25.31	30.79	36.79	32.95	29.76	33.97	29.42	31.71	
Ours-1.4G	34.66	25.30	30.82	36.36	32.96	29.75	33.98	29.29	31.64	
Ours-0.4G	32.92	24.82	30.07	36.06	31.61	28.89	32.19	29.04	30.70	
Ours-0.3G	32.03	24.10	29.42	34.46	30.25	28.44	30.78	27.36	29.60	
	GB \downarrow									
	Chair	Drums	Ficus	Hotdog	Lego	Materials	Mic	Ship	Mean	
Ours-1.9G	0.830	1.240	1.791	2.674	2.067	3.682	0.442	2.689	1.93	
Ours-1.4G	0.671	0.852	0.943	1.495	1.421	3.060	0.569	1.881	1.36	
Ours-0.4G	0.176	0.350	0.287	0.419	0.499	0.295	0.327	1.195	0.44	
Ours-0.3G	0.131	0.183	0.286	0.403	0.340	0.503	0.159	0.381	0.30	
	FPS \uparrow									
	Chair	Drums	Ficus	Hotdog	Lego	Materials	Mic	Ship	Mean	
Ours-1.9G	352.4	175.9	85.6	95.5	186.8	64.2	324.9	56.0	167.7	
Ours-1.4G	399.7	222.2	147.3	163.5	247.9	68.0	393.8	75.4	214.7	
Ours-0.4G	639.6	290.0	208.7	273.5	339.0	268.0	522.6	86.7	328.5	
Ours-0.3G	767.6	424.1	203.8	271.7	443.6	189.1	796.4	181.1	409.7	

Table 7: **Per-scene quantitative results on PlenOctree conversion ablations.**

	PSNR \uparrow									
	Chair	Drums	Ficus	Hotdog	Lego	Materials	Mic	Ship	Mean	
NeRF-SH9	33.88	25.24	30.69	36.68	32.73	29.53	33.68	29.11	31.44	
NeRF-SH16	33.98	25.17	30.72	36.75	32.77	29.95	34.04	29.21	31.57	
NeRF-SH25	34.01	25.10	30.52	36.83	32.76	30.06	34.08	29.11	31.56	
NeRF-SG25	34.08	25.40	31.21	36.92	32.93	29.77	34.31	29.28	31.74	
PlenOctree-SH9	34.38	25.34	30.72	36.68	32.79	29.16	33.23	29.28	31.45	
PlenOctree-SH16	34.66	25.31	30.79	36.79	32.95	29.76	33.97	29.42	31.71	
PlenOctree-SH25	34.72	25.32	30.68	36.96	32.85	29.79	33.90	29.29	31.69	
PlenOctree-SG25	34.37	25.52	31.16	36.67	32.98	29.41	33.63	29.32	31.63	
	SSIM \uparrow									
	Chair	Drums	Ficus	Hotdog	Lego	Materials	Mic	Ship	Mean	
NeRF-SH9	0.973	0.928	0.968	0.978	0.966	0.948	0.984	0.864	0.951	
NeRF-SH16	0.974	0.927	0.968	0.978	0.966	0.951	0.985	0.866	0.952	
NeRF-SH25	0.973	0.926	0.967	0.978	0.966	0.952	0.985	0.864	0.951	
NeRF-SG25	0.974	0.930	0.971	0.978	0.967	0.951	0.986	0.867	0.953	
PlenOctree-SH9	0.980	0.934	0.970	0.982	0.970	0.950	0.984	0.881	0.956	
PlenOctree-SH16	0.981	0.933	0.970	0.982	0.971	0.955	0.987	0.884	0.958	
PlenOctree-SH25	0.981	0.935	0.971	0.983	0.971	0.955	0.987	0.883	0.958	
PlenOctree-SG25	0.980	0.937	0.973	0.982	0.972	0.953	0.986	0.883	0.958	
	LPIPS \downarrow									
	Chair	Drums	Ficus	Hotdog	Lego	Materials	Mic	Ship	Mean	
NeRF-SH9	0.037	0.086	0.043	0.044	0.042	0.063	0.023	0.180	0.065	
NeRF-SH16	0.037	0.087	0.039	0.041	0.041	0.060	0.021	0.177	0.063	
NeRF-SH25	0.038	0.087	0.039	0.040	0.041	0.061	0.021	0.179	0.063	
NeRF-SG25	0.036	0.083	0.034	0.042	0.041	0.060	0.020	0.176	0.062	
PlenOctree-SH9	0.023	0.075	0.041	0.034	0.036	0.068	0.025	0.146	0.056	
PlenOctree-SH16	0.022	0.076	0.038	0.032	0.034	0.059	0.017	0.144	0.053	
PlenOctree-SH25	0.023	0.072	0.036	0.031	0.034	0.060	0.017	0.145	0.052	
PlenOctree-SG25	0.023	0.069	0.034	0.033	0.033	0.064	0.019	0.144	0.052	
	GB \downarrow									
	Chair	Drums	Ficus	Hotdog	Lego	Materials	Mic	Ship	Mean	
PlenOctree-SH9	0.45	0.67	1.15	1.27	1.16	1.48	0.16	1.67	1.00	
PlenOctree-SH16	0.83	1.24	1.79	2.67	2.07	3.68	0.44	2.69	1.93	
PlenOctree-SH25	1.30	1.97	2.57	3.80	3.61	4.04	0.55	3.61	2.68	
PlenOctree-SG25	1.03	1.68	2.43	2.66	2.66	4.44	0.49	2.71	2.26	
	FPS \uparrow									
	Chair	Drums	Ficus	Hotdog	Lego	Materials	Mic	Ship	Mean	
PlenOctree-SH9	521.1	255.6	116.7	183.0	275.1	132.3	519.4	90.6	261.7	
PlenOctree-SH16	352.4	175.9	85.6	95.5	186.8	64.2	324.9	56.0	167.7	
PlenOctree-SH25	269.2	126.7	67.0	66.4	127.1	48.9	279.2	41.3	128.2	
PlenOctree-SG25	306.6	151.9	74.1	104.3	153.3	51.0	294.2	69.6	150.6	

Table 8: Per-scene quantitative results on spherical basis function ablations.